# Electrically pumped hybrid evanescent Si/InGaAsP lasers

**Xiankai Sun, Avi Zadok,* Michael J. Shearn, Kenneth A. Diest, Alireza Ghaffari, Harry A. Atwater, Axel Scherer, and Amnon Yariv**

*Department of Applied Physics, MC 128-95, California Institute of Technology, Pasadena, California 91125, USA*
*Corresponding author: avizadok@caltech.edu*

Received January 22, 2009; revised March 16, 2009; accepted March 26, 2009;
posted March 30, 2009 (Doc. ID 106493); published April 21, 2009

Hybrid Si/III–V, Fabry–Perot evanescent lasers are demonstrated, utilizing InGaAsP as the III–V gain material for the first time to our knowledge. The lasing threshold current of 300-$\mu$m-long devices was as low as 24 mA, with a maximal single facet output power of 4.2 mW at 15°C. Longer devices achieved a maximal single facet output power as high as 12.7 mW, a single facet slope efficiency of 8.4%, and a lasing threshold current density of 1 kA/cm$^2$. Continuous wave laser operation was obtained up to 45°C. The threshold current density, output power, and efficiency obtained improve upon those of previously reported devices having a similar geometry. Facet images indicate that the output light is largely confined to the Si waveguide.
© 2009 Optical Society of America
*OCIS codes:* 250.5960, 250.5300.

A monolithic integration of lasers together with Si integrated electronic circuits has been highly sought after for decades. Unfortunately, Si is a poor converter of electricity to light, due to its indirect semiconductor bandgap. In addition, the epitaxial growth of standard GaAs and InP based direct bandgap materials on Si substrates has proved to be a major obstacle, due to the mismatch in lattice constants and in thermal expansion coefficients [1]. Despite these difficulties, recent years witnessed a reawakening of the interest in Si-integrated lasers, pursued primarily to support high-rate interchip and intrachip communication within multiprocessor computers [2].

Numerous avenues have been followed towards obtaining Si-integrated lasers, including Raman amplification [3], rare-earth doping [4], and nanocrystalline Si structures [5]. One particularly successful approach is based on wafer bonding of AlGaInAs material on top of a prepatterned Si-on-insulator (SOI) wafer [6–8]. The bonded structure is designed to support a joint optical mode, whose profile overlaps both materials. Using this technology, the AlGaInAs layers, which include multiple quantum wells, could be patterned postbonding to produce Fabry–Perot (FP) [6], racetrack [7], and distributed feedback lasers [8], the outputs of which are predominantly emitted from the underlying Si waveguides. The modal gain is obtained by the evanescent tail of the joint mode, which penetrates into the multiple quantum wells. The devices are referred to as evanescent hybrid Si/AlGaInAs lasers [6]. A similar approach is implemented in Si-coupled microdisk lasers [9], although their output power is limited to tens of $\mu$W.

The AlGaInAs material system is advantageous in uncooled laser operation at high temperatures, due to the large conduction band offset [10]. On the other hand, high-quality AlGaInAs layers are relatively more difficult to obtain, and the reliability of Al-containing lasers remains a concern [10,11]. In addition, Al alloys are prone to nonradiative surface recombination, which may elevate the lasing threshold current. In this work, we demonstrate hybrid Si/III–V, evanescent FP lasers based on a different III–V material system, i.e., InGaAsP quaternary compounds. We find that the threshold current density and the threshold voltage of the fabricated devices are 30–40% lower than those of the corresponding, previously reported FP devices [6]. As one of the key challenges facing hybrid Si/III–V active devices is the extent of heat generation [12], the reduction in threshold current and voltage may prove significant. At the same time, the output power and differential slope efficiency observed are higher than previously reported.

The hybrid Si/III–V structure consists of an SOI wafer and an InGaAsP wafer that were bonded together. The thicknesses of the buried $SiO_2$ layer and the undoped Si device layer were 2.0 $\mu$m and 0.9 $\mu$m, respectively. A waveguide was defined in the Si device layer using electron beam lithography and subsequent $SF_6/C_4F_8$ plasma reactive ion etching. The waveguide width ranged between 0.9 $\mu$m and 1.3 $\mu$m. The Si to the two sides of the waveguide was entirely etched, down to the $SiO_2$ layer. After etching, the SOI wafer was cleaned by solvents and a 3:1 $H_2SO_4:H_2O_2$ mixture (10 min at 170°C). The details of the key structural layers of the InGaAsP wafer, grown on top of a 350-$\mu$m-thick InP substrate, are provided in Table 1. The wafer design guidelines closely follow those of [6], albeit in a different material system.

The bonding procedure began with solvent cleaning of both surfaces. A 10-nm-thick oxide layer was grown on top of the patterned SOI wafer to enhance the bonding strength. The surfaces of the wafers were then activated through exposure to oxygen plasma and bonded together under a pressure of 0.1 MPa at 350°C for 1 h. Low temperature, plasma-assisted bonding was shown to be a powerful tool for integrating dissimilar material systems [6,13].

Following the bonding, the InP substrate was removed by HCl wet etching. An 80-$\mu$m-wide mesa structure was formed in the InGaAsP layers, cen-

**Table 1. InGaAsP Wafer Epilayer Structure**

| Layer | Material | Thickness (nm) | Bandgap (eV) | Doping ($cm^{-3}$) |
|---|---|---|---|---|
| *p*-side contact layer | $p$-$In_{0.53}Ga_{0.47}As$ | 200 | 0.77 | $p>10^{19}$ |
| Upper cladding layer | *p*-InP | 1500 | 1.34 | $p=10^{18}\rightarrow 5\times 10^{17}$ |
| Separate confinement layers | InGaAsP | 40 | 1.08 | undoped |
| | InGaAsP | 40 | 0.99 | undoped |
| Quantum wells (1% compressive strain) | InGaAsP (×5) | 7 | 0.83 | undoped |
| Barriers (0.3% tensile strain) | InGaAsP (×4) | 10 | 0.99 | undoped |
| Separate confinement layers | InGaAsP | 40 | 0.99 | undoped |
| | InGaAsP | 40 | 1.08 | undoped |
| *n*-side contact layer | *n*-InP | 110 | 1.34 | $n=10^{18}$ |
| Superlattice | *n*-InGaAsP (×2) | 7.5 | 1.13 | $n=10^{18}$ |
| | *n*-InP (×2) | 7.5 | 1.34 | $n=10^{18}$ |
| Bonding layer | *n*-InP | 10 | 1.34 | $n=10^{18}$ |

tered above the Si waveguide, through photolithography and subsequent three-phase wet etching, down to the *n*-InP contact layer (see Table 1). The etching solutions were (a) 1:1:10 mixture of $H_2SO_4$:$H_2O_2$:$H_2O$ (*p*-InGaAs layer, 60 s), (b) 2:1 mixture of HCl:$H_2O$ (*p*-InP layer, 30 s), and (c) 1:1:10 mixture of $H_2SO_4$:$H_2O_2$:$H_2O$ (quaternary layers, 4 min). Metal contacts were deposited for the *p* side (Cr/AuZn/Au) on top of the remaining *p*-InGaAs layer, and for the *n*-side (Cr/AuGe/Au) on the exposed *n*-InP layer to the two sides of the mesa. The current flow was laterally confined to a 5-$\mu$m-wide channel by means of proton implantation on its two sides [14]. The implantation dosage and proton energy were $5\times 10^{14}$ $cm^{-2}$ and 170 keV, respectively. Finally, the Si substrate was lapped down to a thickness of 50 $\mu$m, and device bars were cleaved and annealed at 410°C for 10 s. The annealing assists in the diffusion of Zn from the *p*-side metal contact into the *p*-side layers, and therefore reduces the resistance of that region. Figure 1 shows a top view optical microscope image and scanning electron microscope (SEM) images of the device's cross section.

Figure 2(a) shows the output power and device voltage versus current (L–I–V curve) of a 960-$\mu$m-long device, mounted on a thermoelectric cooler at 15°C. The turn-on voltage was 0.8 V, and the lasing threshold voltage $V_{th}$ was 1.3 V. The threshold current $I_{th}$ was 60 mA, corresponding to a threshold current density $J_{th}$ of 1.25 kA/$cm^2$. The maximum power output $P_{max}$ from a single facet was 12.5 mW, and the differential slope efficiency $\eta_{diff}$ for a single facet was 8.4%. The series resistance of the laser was 8Ω. The inset of Fig. 2(a) shows $I_{th}$ as a function of temperature. Continuous wave lasing was achieved at temperatures up to 45°C, and the characteristic temperature of the device was found to be 39°K. Figure 2(b) shows the laser spectrum, whose central wavelength was 1490 nm. The modal loss $\alpha_i$ was estimated as 28 $cm^{-1}$, using Hakki–Paoli measurements below the bandgap [15]. The measured values of $\eta_{diff}$ and $\alpha_i$ correspond to an internal quantum efficiency of 0.54. $J_{th}$ of 1–1.5 kA/$cm^2$ were obtained for numerous devices, having lengths ranging between 300 and 1500 $\mu$m. $I_{th}$ of the 300-$\mu$m-long devices was 24 mA at 15°C, with $P_{max}$ of 4.2 mW. $J_{th}$ and $V_{th}$ of the devices are about 35% lower than those of previously reported FP hybrid Si/AlGaInAs lasers [6]. At the same time, the devices' $P_{max}$ is 70% higher, and their $\eta_{diff}$ is 30% higher. At this stage, we cannot yet

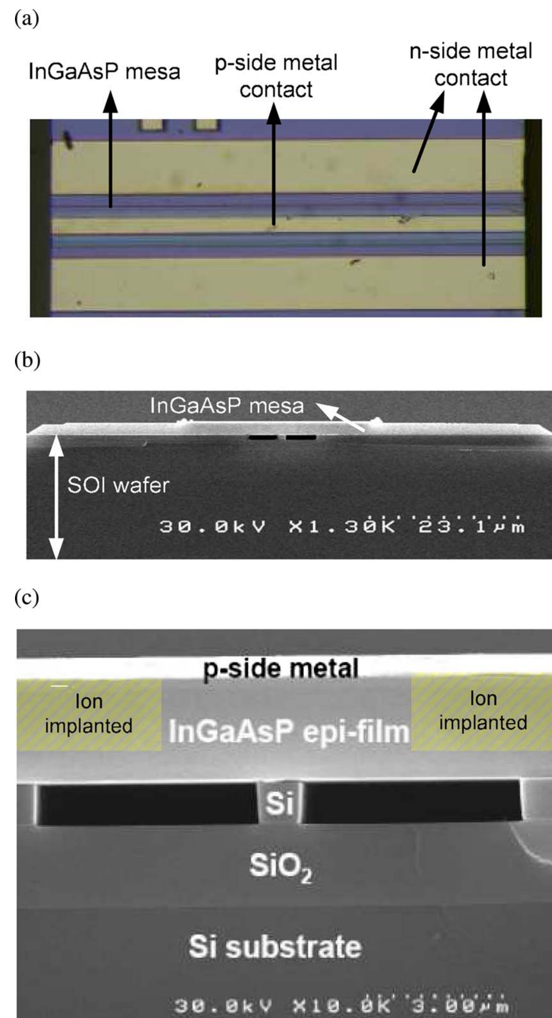


Fig. 1. (Color online) (a) Top view of a fabricated device. (b) SEM overview of a cross section of the device. (c) SEM close-up view of the device cross section at the Si waveguide region. Approximate ion implanted regions are superimposed on the image for illustration.

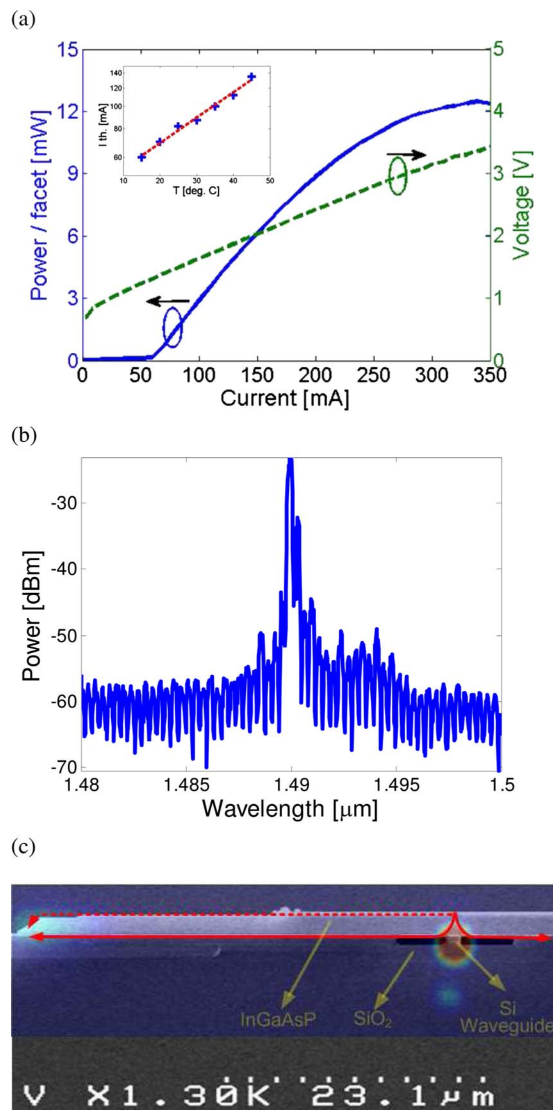


Fig. 2. (Color online) (a) L–I–V curve of a 960-$\mu$m-long laser under cw operation at 15°C. Inset, lasing threshold current (mA, log scale) as a function of temperature (°C) (+), alongside a linear fit (dashed line). (b) Laser spectrum, dB scale. (c) Image of the lasing mode, superimposed upon a scaled SEM cross-sectional view of the device. The solid lines indicate the main current paths from the $p$ side towards the $n$ side, as defined by the ion implantation. The dashed line indicates a residual leakage current path.

determine whether the improved performance is due to the choice of gain material or due to other fabrication related differences.

A high-resolution image of the laser beam is shown in Fig. 2(c), superimposed on a scaled SEM cross-sectional image of the device. The high-intensity beam (red online) overlaps the silicon waveguide. Another spot, whose intensity is 15% of that of the main beam, appears at the left-hand sidewall. Since the current confinement induced by the ion implantation is not complete, low residual currents may flow along the highly doped $p$-InGaAs layer towards the edge of the mesa, and then down towards the $n$-side contact (see the figure). Although negligible in most devices, the current leakage was sufficient to generate the secondary beam in this specific example. Though generally undesirable, this beam was useful in the proper vertical alignment of the two images. Another weak spot below the silicon waveguide, whose intensity is 10% of that of the main beam, is due to a diffraction pattern. The image provides a striking illustration to the confinement of the lasing mode in the Si waveguide [6,16]. Ongoing work focuses on the "supermode control" of the optical confinement along the laser cavity. Such control is expected to provide significant further improvement in device performances [16].

This work was supported by Defense Advanced Research Projects Agency (DARPA) contracts N66001-07-1-2058 and HR0011-04-1-0054, the U.S. Air Force Office of Scientific Research (AFOSR) Grant FA9550-06-1-0480, and the Center for Science and Engineering of Materials, a National Science Foundation (NSF) Materials Research Science and Engineering Center at Caltech. The authors thank the Kavli Nano-Institute, Caltech, for supporting fabrication. A. Zadok acknowledges postdoctoral fellowships from the Center for the Physics of Information, Caltech, and the Rothschild fellowship from Yad-Hanadiv Foundation, Israel. M. J. Shearn thanks the NSF Graduate Research Fellowship program.

## References

1. H. Kromer, T.-Y. Liu, and P. M. Petroff, J. Cryst. Growth **95**, 96 (1989).
2. B. Jalali, Nat. Photonics **1**, 193 (2007).
3. O. Boyraz and B. Jalali, Opt. Express **12**, 5269 (2004).
4. S. Lombardo, S. U. Campisano, G. N. van den Hoven, A. Cacciato, and A. Polman, Appl. Phys. Lett. **63**, 1942 (1993).
5. L. Pavesi, L. Dal Negro, C. Mazzoleni, G. Franzo, and F. Priolo, Nature **408**, 440 (2000).
6. A. W. Fang, H. Park, O. Cohen, R. Jones, M. J. Paniccia, and J. E. Bowers, Opt. Express **14**, 9203 (2006).
7. A. W. Fang, R. Jones, H. Park, O. Cohen, O. Raday, M. J. Paniccia, and J. E. Bowers, Opt. Express **15**, 2315 (2007).
8. A. W. Fang, E. Lively, Y.-H. Kuo, D. Liang, and J. E. Bowers, Opt. Express **16**, 4413 (2008).
9. J. Van Campenhout, P. Rojo Romero, P. Regreny, C. Seassal, D. Van Thouhrout, S. Verstyuft, L. Di Cioccio, J.-M. Fedeli, C. Lagahe, and R. Baets, Opt. Express **15**, 6744 (2007).
10. C.-E. Zah, R. Bhat, B. N. Pathak, F. Favire, W. Lin, M. C. Wang, N. C. Andreadakis, D. M. Huang, M. A. Koza, T.-P. Lee, Z. Wang, D. Darby, D. Flanders, and J. J. Hsieh, IEEE J. Quantum Electron. **30**, 511 (1994).
11. M. Fukuda, *Optical Semiconductor Devices* (Wiley, 1999), Chap. 7.
12. M. N. Sysak, H. Park, A. W. Fang, J. E. Bowers, R. Jones, O. Cohen, O. Radai, and M. J. Paniccia, Opt. Express **15**, 15041 (2007).
13. D. Pasquariello and K. Hjort, IEEE J. Sel. Top. Quantum Electron. **8**, 118 (2002).
14. H. Boudinov, H. H. Tan, and C. Jagadish, J. Appl. Phys. **89**, 5343 (2001).
15. L. J. P. Ketelsen, Electron. Lett. **30**, 1422 (1994).
16. X. K. Sun and A. Yariv, J. Opt. Soc. Am. B **25**, 923 (2008).